Amyloidogenesis of bacterial prionoid RepA-WH1 recapitulates dimer to monomer transitions of RepA in DNA replication initiation

Eva Torreira[1$], María Moreno[1$], Maria Eugenia Fuentes-Perez[2], Cristina Fernández[1], Jaime Martín-Benito[2], Fernando Moreno-Herrero[2], Rafael Giraldo[1]*, Oscar Llorca[1]*

[1] Centro de Investigaciones Biológicas, Consejo Superior de Investigaciones Científicas (CSIC), Ramiro de Maetzu 9, 28040 Madrid, Spain

[2] Centro Nacional de Biotecnología, Consejo Superior de Investigaciones Científicas (CSIC), Darwin 3, 28049 Madrid, Spain

Running Title: Structure of RepA-WH1 amyloid filaments

[$] Shared first authorship

* Co-corresponding authors:

Prof. Oscar Llorca
Tel +34 91 837 31 12 ext 4446
E-mail: ollorca@cib.csic.es

Prof. Rafael Giraldo
Tel: +34 91 837 31 12 ext 4348
E-mail: rgiraldo@cib.csic.es

SUMMARY

Keywords: RepA / RepA-WH1 prionoid / amyloid protofilaments / amyloid assembly / electron microscopy

Most available structures of amyloids correspond to peptide fragments that self-assemble in extended cross β-sheets. However, structures in which a whole protein domain acts as building block of an amyloid fiber are scarce, in spite of their relevance to understand amyloidogenesis. Here we use electron microscopy (EM) and atomic force microscopy (AFM) to analyze the structure of amyloid filaments assembled by RepA-WH1, a winged-helix domain from a DNA replication initiator in bacterial plasmids. RepA-WH1 functions as a cytotoxic bacterial prionoid that recapitulates features of mammalian amyloid proteinopathies. RepA are dimers that monomerize at the origin to initiate replication, and we find that RepA-WH1 reproduces this transition to form amyloids. RepA-WH1 assembles double helical filaments by lateral association of a single-stranded precursor built by monomers. Double filaments then associate in mature fibers. The intracellular RepA-WH1 aggregates killing bacteria might reproduce the hierarchical assembly of human amyloidogenic proteins.

Introduction

Rep proteins constitute a family of DNA replication initiators found in Gram-negative bacterial plasmids (Giraldo and Fernandez-Tresguerres, 2004). Encoded in the *Pseudomonas* plasmid pPS10, RepA consists of two 'winged-helix' (WH) domains, WH1 and WH2 (**Figure 1A**). Although the structure of full-length RepA has not been solved, those of a dimer of the N-terminal WH1 domain of RepA (Giraldo et al., 2003)

and the full-length RepE54 monomer, a related replication initiation protein (Giraldo and Fernandez-Tresguerres, 2004; Komori et al., 1999), have been used to model RepA (Giraldo and Fernandez-Tresguerres, 2004). Similarly to other proteins in the Rep family, monomers of RepA initiate plasmid DNA replication whereas RepA dimers function as transcriptional repressors at the operator of the *repA* gene (**Figure 1A**) (Giraldo et al., 1998). RepA dimers are formed by the interaction between the N-terminal WH1 domains, as revealed in the atomic structure of a dimer consisting of two WH1 domains (PDB ID 1HKQ) (Giraldo et al., 2003) (**Figure 1B**), whereas additional evidence indicates that the WH2 domain drives sequence-specific DNA binding (Giraldo et al., 1998). Current models propose that the dissociation of RepA dimers into monomers is promoted by binding to specific DNA sequences at the plasmid replication origin, eliciting a conformational change that affects the N-terminal WH1 dimerization domain (Diaz-Lopez et al., 2006; Diaz-Lopez et al., 2003; Giraldo et al., 2003). Moreover, complexes involving monomeric Rep proteins, the specific Rep-binding sites, and a ssDNA from the AT-rich region at the origin are critical for the initiation of plasmid replication (Wegrzyn et al., 2014). Upon completion of DNA replication, the two resulting plasmid copies remain associated through their replication origins by a bridge established by a core of RepA monomers, which are coupled through interactions mediated by their WH1 domains (Gasset-Rosa et al., 2008b). This mechanism (termed 'handcuffing') negatively regulates, through steric hindrance, the firing of premature new replication rounds (Chattoraj, 2000) (**Figure 1A**).

A truncated version of RepA that comprises the WH1 domain only has been shown to assemble as amyloid fibers upon binding to short, specific dsDNA sequences *in vitro* (Gasset-Rosa et al., 2008a; Giraldo, 2007) (**Figure 1A-1B**). The introduction of

a single point mutation (A31V) identified in searches for RepA variants with increased affinity for other proteins in the replication machinery, and which enables pPS10 to replicate in an expanded range of bacterial hosts (Giraldo and Fernandez-Tresguerres, 2004), enhanced the efficiency of amyloid formation (Giraldo, 2007). This protein, RepA-WH1(A31V) (for simplicity, referred henceforth as RepA-WH1), which as the wild-type formed dimers in solution (Giraldo, 2007; and **Figure S1**), assembled amyloid fibers of 25 nm width, only in the presence of a dsDNA sequence matching the spacer between inverted repeats at the *repA* operator (Giraldo, 2007) (**Figure 1A**). RepA-WH1 fibers have been characterized using several methods, including circular dicroism (CD), X-ray fiber diffraction and differential spectral absorption upon binding of Congo Red (Giraldo, 2007).

Protein amyloid aggregates are involved in the etiology of human neurodegenerative and systemic diseases, but they also function as epigenetic determinants of selectable phenotypes (Toyama and Weissman, 2011; Chiti and Dobson, 2006). This opened an intense research to gain understanding on the structural basis of amyloid assembly, but this objective is challenged by their polymorphic nature, ranging from small soluble oligomers to large fibers (Eichner and Radford, 2011). Although not directly involved in any human disease, RepA-WH1 is a good model system to study amyloid proteinopathies elicited by proteins starting from a properly folded, compact 3D fold, rather than from intrinsically disordered states or small peptides (Giraldo et al., 2011). There are noticeable similarities between the mammalian prion protein PrP and RepA-WH1, including that both have nucleic acids and lipids as effectors of amyloidosis (Silva et al., 2010; Wang et al., 2010; and our own unpublished findings on RepA-WH1). Interestingly, intracellular RepA-WH1 aggregates cause an

amyloid proteinopathy in *E. coli* that is propagated from mother to daughter cells, slows significantly cell division rates, and are able to seed the growth of amyloid fibers *in vitro* (Fernandez-Tresguerres et al., 2010), recapitulating many of the features of amyloidosis in yeast and mammalian cells, including the existence of strain-like conformational variants (Gasset-Rosa et al., 2014).

The three-dimensional (3D) structures of the peptide cores of several amyloids have been solved using X-ray crystallography (Liu et al., 2011: Ivanova et al., 2009) or solid state NMR (Fitzpatrick et al., 2013; Antzutkin et al., 2000), whereas the structures of large amyloid fibrillar assemblies are typically solved, at lower resolutions, through single particle electron microscopy (EM) and helical reconstruction methods (Arranz et al., 2012; Mizuno et al., 2011; Sachse et al., 2010). So far, most of the 3D-structures solved for amyloids correspond to assemblies of peptide fragments (Eisenberg and Jucker, 2012), such as Alzheimer's Aβ(1-40/42) (Fandrich et al., 2011) and the prion domain in HET-s(218-289) (Wasmer et al., 2008). However, fibers built on full-length protein molecules are also amenable to structural analyses, as for insulin (Ivanova et al., 2009), β2-microglobulin (Liu et al., 2011) and SOD1 (Elam et al., 2003), or the PI3K-SH3 (Jimenez et al., 1999) and HypF-N (Campioni et al., 2012) domains. In those cases in which the amyloidogenic proteins have stable 3D-folds, a relevant issue is whether the protein molecules acting as building blocks in the crossed-β sheets undergo a radical unfolding or not, i.e., they partially and transiently expose just an amyloidogenic peptide sequence for assembly (Chiti and Dobson, 2009). Examples of the former are insulin (Ivanova et al., 2009) and β2-microglobulin (Liu et al., 2011), whereas SOD1 (Elam et al., 2003) and HypF-N (Campioni et al., 2012) fit to the latter.

Here we have used RepA-WH1 to study a mechanism involved in the assembly of amyloid fibers by stable domains, using EM and Atomic Force Microscopy (AFM), and we find that RepA-WH1 dimers have to dissociate into monomers to assemble helical filaments. These filaments associate into double helical structures that further associate laterally into thicker fibers, whose variable degree of twisting results in structural polymorphism. RepA-WH1 domain is structurally unrelated to any protein involved in human disease but yet, once assembled as a prionoid, it elicits an amyloid proteinopathy in bacteria (Gasset-Rosa et al., 2014; Fernandez-Tresguerres et al., 2010). As reported here, the finding that RepA-WH1 recapitulates the hierarchical assembly of amyloids in human neurodegenerative and systemic diseases further qualifies this bacterial prionoid as a relevant model system to approach the structural basis of amyloid proteinopathies.

Results

RepA-WH1 amyloid fibers are assembled by association of filaments

Earlier electron microscopy studies suggested that RepA-WH1 amyloid fibers assembled by the hyper-amyloidogenic mutant A31V could be obtained through allosteric binding of a dsDNA oligonucleotide effector (Giraldo, 2007) or by seeding with purified amyloid aggregates generated within *E. coli* (Fernandez-Tresguerres et al., 2010) (**Figure 1A**). A recent report demonstrated that aggregates of Alzheimer's Aβ(1-40/42) extracted from biological samples do template *in vitro* the growth of amyloid fibers with the very same conformation found *in vivo* (Lu et al., 2013). Thus, a similar seeding procedure was chosen to grow RepA-WH1 fibers for our structural analyses.

We first purified RepA-WH1, which behaved as a dimer in solution (**Figure S1**), as reported before (Giraldo, 2007; Giraldo et al., 2003), whereas seeds were obtained from purified RepA-WH1 aggregates generated in the cytoplasm of *E. coli*. EM revealed that RepA-WH1 amyloid fibers grew from this globular, proteotoxic aggregates (**Figure 1C, i**), showing various widths and degrees of twisting (**Figure 1C, ii**). Mechanical shearing in a buffer with reduced ionic strength resulted in fraying of fiber ends (**Figure 1C, iii**), and ultimately, in dissociation of their constituent filaments (**Figure 1C, iv**), revealing that fibers were built from the association of several filament units. We were unable to successfully visualize these preparations after vitrification and observation under liquid nitrogen temperatures (cryo-EM) since the buffer used for assembly of the fibers and filaments was not compatible with cryo-EM. Also, we were unsuccessful in exchanging this buffer whilst maintaining filament integrity. Further work will be required to address these issues.

RepA-WH1 amyloidogenesis and fiber assembly, triggered using dsDNA, had been characterized before by circular dichroism (CD) (Giraldo, 2007). In this study, we have explored the kinetics of fiber assembly by CD (**Figure 1D**), but this time using intracellular bacterial RepA-WH1 aggregates purified *ex vivo* as nucleation seeds, since this method was used in the generation of the fibers analyzed by EM (see above) and AFM (see below). The experiment revealed that the spectrum of RepA-WH1 progressively acquired the typical profile of a protein enriched in β-sheets (a broad ellipticity minimum at c.a. 215 nm), at the expense of the α-helical minima (i.e., 208 and 222 nm). This observation is particularly evident when RepA-WH1 was seeded with purified intracellular aggregates of the prionoid (**Figure 1D, ii**), relative to the spectra reflecting the spontaneous long-term aggregation of the protein (**Figure 1D, i**),

which typically renders amorphous aggregates (Giraldo, 2007). In addition, aggregation kinetics (i.e., the rate of increase in ellipticity signal) is speeded-up in the seeded sample.

RepA-WH1 fibers were also analyzed by AFM, which revealed a clear left-handed helical structure. RepA-WH1 fibers displayed large heterogeneity in height and length. For each fiber we measured the height values for the peaks and valleys, confirming that fibers were very variable (**Figure S2**, **Table S1**). The most abundant population showed heights of 16 ± 2 nm and 13 ± 2 nm measured at the peak and valley positions, respectively (**Figure 2A**, profile 1). The mean pitch size inferred from these fibers was 64 ± 6 nm. A less abundant population of higher fibers (i.e., those with brighter contrast) was also observed (**Figure S2**, **Table S1**). These fibers displayed approximately twice the height of the smaller ones, ranging from 20 to 27 nm, with mean values of 25 ± 2 nm (peaks) and 21 ± 2 nm (valleys) (**Figure 2A**, profile 2). We observed a large variability of heights within each population, and even within a single fiber, suggesting that fibers are composed of smaller filamentous constituents. Polymorphism in the degree of twisting and pitch is a common feature in amyloid fibers (Diaz-Avalos et al., 2005). The constituent filaments in each fiber were observed after shearing, as revealed by EM (**Figure 1C**). Indeed, AFM images also showed several short filament-like structures arising from the end of some fibers (**Figure 2B**). These filaments were homogeneous in height with a mean value of 3.9 ± 0.3 nm (**Figure 2B**, profile 3). We could not assign any helicity to these filaments since they were often too short and at the limit of the resolution of the technique.

RepA-WH1 forms single and double helical amyloid filaments

The constituent filaments forming the RepA-WH1 fibers were sufficiently thin to be studied through single particle and helical reconstruction methods in EM. These filaments were visible at the ends of the fibers but also dispersed across the micrographs as individual units (**Figure 3A**). We boxed 19,300 segments along the isolated filaments in the micrographs, each segment covering approximately 36 nm in length (**Figure 3B**). 2,277 segments from those filaments at the end of the fibers were also extracted and both sets of images were analyzed independently. Images were then aligned and classified using single-particle image processing methods to group similar images, obtaining averages with improved signal to noise ratio (**Figure 3B**). These averages revealed several well-defined helical structures, which could be assigned to two main sub-types by visual inspection, which were later found to correspond to either single or double filaments (**Figure 3B**). Within each of these two groups, averages revealed several degrees of bending and stretching, an indication of conformational heterogeneity within the segments of each filament and/or between filaments. Importantly, we observed similar averages for the isolated filaments and those filaments observed at the ends of fibers, further supporting that fibers are assembled by the interaction of these simpler units. We thus concentrated our efforts in the free filaments, which were the most abundant species in our data set. Images of single filaments were only detected in isolation and never as part of the fiber ends, which, based on their 3D structure (see below), could indicate that these single filaments are intermediates in the pathway for the assembly of the double filaments and the fibers.

We applied the iterative helical real space reconstruction (IHRSR) method to images of single and double filaments to resolve their structure (Egelman, 2007). Refinement experiments using images from several classes did not converge, suggesting

that the conformational differences between subgroups was sufficiently large to hamper alignment in 3D and convergence. Thus, we applied a variation of the IHRSR method adapted for highly heterogeneous complexes (Arranz et al., 2012), and which uses only the homogenous subset of images from each class average. Each subset was processed independently by applying helical symmetry as described before (Arranz et al., 2012), and curved filaments were discarded from this analysis (**Figure S3**). The two types of averages described corresponded to either a single (**Figure 3C**) or a double filament (**Figure 3D**). To validate these structures, we compared the power spectrum of average images and projections from the 3D structures, which were found to match (**Figure S3**) (Egelman, 2007). In addition, projections of the structures matched better with reference-free averages obtained for images of the same conformation, compared to the match with images of slightly different conformations (**Figure S3**).

RepA-WH1 amyloids consist of assembled monomers

RepA forms dimers in solution that convert into monomers upon activation (Giraldo et al., 2003), and RepA-WH1 is also a dimer (**Figure S1**). Thus an important question was to address whether monomeric or dimeric units of RepA-WH1 were the constituents of the filaments. For this purpose, both the single and the double filaments were segmented into their elemental units, using UCSF Chimera and allowing the maximum number of segments (Pettersen et al., 2004). This unbiased segmentation revealed the units that reconstitute the whole structure upon repetition using the helical symmetry (**Figure S3**). Further segmentation would have generated segments smaller than a RepA-WH1 monomer whereas larger segments would include two parts of the helix related by helical symmetry. However, in the dimer, two monomers of WH1 are not

related by helical symmetry but through a pseudo-two fold axis (Giraldo et al., 2003) (**Figure 1B**).

When fitting between the crystal structure of RepA-WH1 into each segment as defined by EM was attempted (**Figure 3C-E**), we found that dimers could not fit the EM structures of single and double filaments since dimers were significantly larger than the segment. On the other hand, the structure of a monomer of RepA-WH1 fitted convincingly within the EM density (single filaments: cross-correlation = 0.89 for monomer; 0.84 for dimer; double filaments: cross-correlation = 0.95 for monomer; 0.89 for dimer) (**Figure 3E**). Due to the resolution of our map and the globular shape of the monomer the precise orientation of RepA-WH1 within the EM structure could not be defined unambiguously. For the same reason, the hand used to represent the structure is arbitrary. To discard any effect of the segmentation, we also tried to fit the dimer into the complete filament by searching the match of a RepA-WH1 dimer within the unsegment structures. We did not find any high correlation solution further indicating that RepA-WH1 dimers are not the constituent element of the amyloid filament. As a whole, these experiments indicated that RepA-WH1 filaments were assembled after the association of monomers, most likely after some structural distortion increasing their β-sheet content (Giraldo 2007; Giraldo et al., 2003) (**Figure 1D**).

Discussion

With the exception of HET-s prion (Wasmer et al., 2008), we still lack a 3D-structure with atomic resolution of any other full-length protein in its amyloid fibrillary state. Here we show that RepA-WH1 assembles single filaments that associate to form double filaments, which are the building units for the amyloid fibers (**Figure 4**). Such

association would imply some kind of interlocked new interactions not present in the single filament. The comparison of the EM structure of these filaments with the atomic structures and models for RepA-WH1 dimers and monomers (Giraldo et al., 2003) indicated that dimers were not compatible with the basic structural unit in RepA-WH1 filaments. Therefore, the most likely model would be that dimers must dissociate into monomers that accommodate some kind of distortion in their path towards amyloid cross-β assembly (**Figure 4**). RepA-WH1 could be a suitable model system to understand protein amyloidogenesis when starting from a properly folded structure (Giraldo et al., 2011).

The structure of RepA-WH1 amyloid filaments allows for some speculation about potential mechanisms of regulation of DNA replication initiation by RepA. Pre-standing experimental evidence on the natural conformational activation of RepA established that, upon binding to specific dsDNA sequences at pPS10 replication origin, protein dimers dissociated into monomers (Diaz-Lopez et al., 2006; Diaz-Lopez et al., 2003). Dimerization of RepA and RepA-WH1 occurs through the WH1 domain (Giraldo et al., 2003), and thus the dimer to monomer transition we observed during amyloidogenesis of RepA-WH1 may possibly replicate to some extent the structural changes occurring in RepA during initiation of DNA replication. Besides triggering DNA replication through the subsequent binding to host factors, RepA becomes then aggregation prone, in such a way that the replication origins from two plasmid molecules become ‘handcuffed’ by ‘gluing’ of RepA monomers, precisely through their amyloidogenic WH1 domain (Gasset-Rosa et al., 2008b) (**Figure 1A**). The RepA-WH1 double filaments described here suggest a possible model for the association of RepA monomers, but this is unlikely identical to the functional structure of RepA aggregates

in handcuffing. There is only a subtle association between the two strands in a double filament, and handcuffing seems to be established on robust intermolecular interactions (Gasset-Rosa et al., 2008b). But the strong interactions between consecutive monomers within the single-stranded filaments could be a better candidate for the structure of handcuffed RepA assemblies. We predict that the presence of the C-terminal WH2 domain in full length RepA would limit the extension of amyloid interactions to the pairwise 'transversal' association of WH1 domains in the DNA-bound protein. On the contrary, in the absence of WH2, such as in the RepA-WH1 prionoid, sterically unrestricted amyloid polymerization would lead to the fibers characterized in this work (**Figure 4**). We speculate that the irreversible aggregation of full length RepA protein upon completion of DNA replication, leading to the inactivation of further replication rounds, may mimic an amyloid assembly.

In summary, we show that the conformational activation of RepA, which is coupled to monomerization to become an efficient DNA replication initiator, and RepA-WH1 amyloidogenesis, which results in cytotoxicity, are two distinct events intimately related with the properties of the WH1 domain. This domain can switch from dimer to monomer, and it can associate in the form of large assemblies. The structure of the fibers assembled by the synthetic bacterial prionoid RepA-WH1 reveals that amyloidogenesis in some globular proteins could require dimer-monomeric transitions, and this may be potentially relevant to human diseases in which the proteins involved have native association states beyond monomers.

Experimental Procedures

Preparation of RepA-WH1 fibers and filaments

RepA-WH1(A31V) protein was purified as described (Giraldo, 2007). Amyloid fibers were assembled *in vitro* with a slight modification of the established protocol (Fernández-Tresguerres et al., 2010; Giraldo, 2007): RepA-WH1(A31V) protein (25µM) was seeded with 1µg of RepA-WH1(A31V)-mRFP aggregates purified from *E. coli* cells in 100 µl aliquots containing 0.1 M Na_2SO_4, 40 mM HEPES pH 8.0, 5 mM $MgSO_4$, 7% PEG 4000, 3% MPD. Samples were left standing still at 5 ^oC for 15 days. This resulted in fibers up to 25 nm Ø wide. To detach their component RepA-WH1(A31V) filaments, fibers were diluted 1:3 to 1:10 in water and then sheared by pipetting five times through a P-10 tip before adsorption on copper grids (for EM) or mica sheets (for AFM).

CD spectroscopy

200-µl samples were made by diluting RepA-WH1(A31V) protein stock to 15 µM in 0.1 M Na_2SO_4 and 40 mM Tris·HCl pH 8, either with or without 1 µg of RepA-WH1(A31V)-mRFP aggregates purified from *E. coli* cells undergoing amyloidosis (Fernández-Tresguerres et al., 2010). Compared with the fibrillation assays (see above), crowding agents (PEG4000/MPD) were omitted from the reactions to gain clearer spectra, albeit at the expense of slower kinetics. Samples were incubated at 4°C and CD spectra were serially acquired every seven days with a Jasco-720 spectropolarimeter using 0.1 cm path-length quartz cuvettes (Hellma). The cell holder was kept at 20°C with a Peltier module and CD spectra were acquired between 260 and 195 nm (20 nm/min scan speed). Ten spectra were averaged for each sample, and the buffer spectrum was subtracted as a blank. Raw data (in mdeg) were converted to mean residue molar ellipticity [θ] ($deg \cdot cm^2 \cdot dmol^{-1}$).

Atomic Force Microscopy (AFM)

Freshly cleaved mica sheets (SPI supplies) were pre-treated with 20 µl of polyl-l-lysine 0.01% solution (sigma) for a few seconds, washed with Milli-Q water and dried with nitrogen gas. Then, the fiber sample, diluted 1:3 in water, was placed onto the pretreated mica. After adsorption for 1 min, the sample was gently washed with Milli-Q water and blown dry in a soft stream of nitrogen gas. Samples were imaged in air at room temperature and low humidity using tapping mode with amplitudes of 5 nm and scan rates of 1 lines·s^{-1} using an AFM from Nanotec (Nanotec Electrónica, Madrid, Spain). We employed AFM tips PointProbePlus (PPP-NCH, Nanosensors, Switzerland) with a nominal tip radius below 10 nm. Image processing consisted in a plane subtraction and flattening. Height and lateral calibrations of the AFM were performed using commercial grids with square pitches of 4 µm length and 25 nm of step height, and in addition, DNA molecules were used as an internal control. From each fiber, three characteristic measurements were taken from the height profile for the peaks and valleys, respectively. We analysed 20 and 5 fibers for the most and less abundant populations, respectively. Only fibers with a visible helicity were measured, as shown in the **Figure 2A**. Broken fibers without a clear helicity pattern were discarded (aprox. 30%). Then, all data was represented in the height histogram and the mean value and the standard deviation obtained for each population was calculated (**Figure S2**, **Table S1**).

Electron microscopy

10 µL samples were adsorbed on glow-discharged 400-mesh copper grids (Ted Pella, Inc.), washed three times and, contrasted with 2% uranyl acetate for 2 min. Specimens were then examined in a JEOL JEM-1230 transmission electron microscope, operating at 100 kV. For those samples used in image processing 5 µl of a 1:3 dilution of RepA-

WH1 (25 µM) at incubation-day 15 were applied to glow-discharge carbon-coated grids for 2 minutes, and stained with 2% (w/v) uranyl formate. Micrographs were recorded under low dose conditions using a TemCam-F416 detector and EM-TOOLS from Tietz Video and Image Processing Systems (TVIPS). Images were collected at a final magnification of 41586×.

Image processing

CTF correction was performed using BSOFT (Heymann and Belnap, 2007). 19333 images selected using EMAN (Ludtke, 2010) were classified using XMIPP (Scheres et al., 2008; Sorzano et al., 2004). 3D refinement was performed using the iterative helical real space reconstruction (IHRSR) method (Egelman, 2007), modified to deal with the heterogeneity of the filaments as described before (Arranz et al., 2012). Classes containing curved filaments were discarded and the rest of the images were re-classified. 3D refinement was performed only for selected averages with a number of images ranging from 200 to 350, and each homogenous subgroup was refined independently. For each of these subgroups an initial 3D-reconstruction was performed with EMAN using a cylinder with the appropriate diameter as a reference (Ludtke, 2010). Cylinders used as template for refinement were obtained using *makeinitialmodel.py* in EMAN (Ludtke, 2010). No-symmetry was applied at this stage during refinement and preliminary helical parameters were determined using the 3D structures obtained. These values were used as initial parameters during the Iterative Helical Real Space Reconstruction (IHRSR) (Egelman, 2007). Refinement of several subgroups of images for double filaments yields similar structures but with small differences in the convergence parameters. A representative class for single and double filaments was then selected for further refinement until convergence. Estimated

parameters for these subgroups were: rise, 12.5 Å and delta-phi, 81 degrees, for single filaments; rise, 23.5 Å and delta-phi, 68.5 degree, for double filaments. Resolution was estimated using the *resolution_ssnr* in Xmipp (Sorzano et al., 2004) as 29 and 28 Å, for single and double filaments respectively. Fitting of RepA-WH1 was performed using UCSF Chimera (Pettersen et al., 2004) after segmentation of single and double filaments. Fitting was carried out on both hands, obtaining similar correlation coefficients, and thus hand selected for representation is arbitrary. For the fitting we used models based on the crystal structure of the RepA-WH1 dimer (PDB ID 1HKQ) (Giraldo et al., 2003) and on the structure of the WH domain of RepE54 (PDB ID 1REP) (Giraldo and Fernandez-Tresguerres, 2004).

To validate the structures we compared the power spectrum of reference-free averages of the images used for the reconstructions of single and double filaments with the power spectrum of projections from the 3D structures. For this, averages and projections were padded to 2048 x 2048 pixels using the *xmipp_transform_window* command in Xmipp (Scheres et al., 2008; Sorzano et al., 2004), and a mask with a raised cosine was applied prior to FFT visualization. In addition, projections from the structures were compared with reference-free averages using the *refine* command in EMAN (Ludtke, 2010). All possible projections were compared with the averages and a quality factor defined by EMAN scores the quality of the match, with higher values indicating a better match (Ludtke, 2010).

References

Antzutkin, O.N., Balbach, J.J., Leapman, R.D., Rizzo, N.W., Reed, J., and Tycko, R. (2000). Multiple quantum solid-state NMR indicates a parallel, not antiparallel,

organization of beta-sheets in Alzheimer's beta-amyloid fibrils. Proceedings of the National Academy of Sciences of the United States of America *97*, 13045-13050.

Arranz, R., Mercado, G., Martin-Benito, J., Giraldo, R., Monasterio, O., Lagos, R., and Valpuesta, J.M. (2012). Structural characterization of microcin E492 amyloid formation: Identification of the precursors. Journal of structural biology *178*, 54-60.

Campioni, S., Mannini, B., Lopez-Alonso, J.P., Shalova, I.N., Penco, A., Mulvihill, E., Laurents, D.V., Relini, A., and Chiti, F. (2012). Salt anions promote the conversion of HypF-N into amyloid-like oligomers and modulate the structure of the oligomers and the monomeric precursor state. Journal of molecular biology *424*, 132-149.

Chattoraj, D.K. (2000). Control of plasmid DNA replication by iterons: no longer paradoxical. Molecular microbiology *37*, 467-476.

Chiti, F., and Dobson, C.M. (2006). Protein misfolding, functional amyloid, and human disease. Annual review of biochemistry *75*, 333-366.

Chiti, F., and Dobson, C.M. (2009). Amyloid formation by globular proteins under native conditions. Nature chemical biology *5*, 15-22.

Diaz-Lopez, T., Davila-Fajardo, C., Blaesing, F., Lillo, M.P., and Giraldo, R. (2006). Early events in the binding of the pPS10 replication protein RepA to single iteron and operator DNA sequences. Journal of molecular biology *364*, 909-920.

Diaz-Lopez, T., Lages-Gonzalo, M., Serrano-Lopez, A., Alfonso, C., Rivas, G., Diaz-Orejas, R., and Giraldo, R. (2003). Structural changes in RepA, a plasmid replication initiator, upon binding to origin DNA. The Journal of biological chemistry *278*, 18606-18616.

Egelman, E.H. (2007). Single-particle reconstruction from EM images of helical filaments. Current opinion in structural biology *17*, 556-561.

Eichner, T., and Radford, S.E. (2011). A diversity of assembly mechanisms of a generic amyloid fold. Molecular cell *43*, 8-18.

Eisenberg, D., and Jucker, M. (2012). The amyloid state of proteins in human diseases. Cell *148*, 1188-1203.

Elam, J.S., Taylor, A.B., Strange, R., Antonyuk, S., Doucette, P.A., Rodriguez, J.A., Hasnain, S.S., Hayward, L.J., Valentine, J.S., Yeates, T.O., *et al.* (2003). Amyloid-like filaments and water-filled nanotubes formed by SOD1 mutant proteins linked to familial ALS. Nature structural biology *10*, 461-467.

Fandrich, M., Schmidt, M., and Grigorieff, N. (2011). Recent progress in understanding Alzheimer's beta-amyloid structures. Trends in biochemical sciences *36*, 338-345.

Fernandez-Tresguerres, M.E., de la Espina, S.M., Gasset-Rosa, F., and Giraldo, R. (2010). A DNA-promoted amyloid proteinopathy in Escherichia coli. Molecular microbiology *77*, 1456-1469.

Fitzpatrick, A.W., Debelouchina, G.T., Bayro, M.J., Clare, D.K., Caporini, M.A., Bajaj, V.S., Jaroniec, C.P., Wang, L., Ladizhansky, V., Muller, S.A., *et al.* (2013). Atomic structure and hierarchical assembly of a cross-beta amyloid fibril. Proceedings of the National Academy of Sciences of the United States of America *110*, 5468-5473.

Gasset-Rosa, F., Coquel, A.S., Moreno-Del Alamo, M., Chen, P., Song, X., Serrano, A.M., Fernandez-Tresguerres, M.E., Moreno-Diaz de la Espina, S., Lindner, A.B., and Giraldo, R. (2014). Direct assessment in bacteria of prionoid propagation and phenotype selection by Hsp70 chaperone. Molecular microbiology *91*, 1070-1087.

Gasset-Rosa, F., Diaz-Lopez, T., Lurz, R., Prieto, A., Fernandez-Tresguerres, M.E., and Giraldo, R. (2008a). Negative regulation of pPS10 plasmid replication: origin pairing by zipping-up DNA-bound RepA monomers. Molecular microbiology *68*, 560-572.

Gasset-Rosa, F., Mate, M.J., Davila-Fajardo, C., Bravo, J., and Giraldo, R. (2008b). Binding of sulphonated indigo derivatives to RepA-WH1 inhibits DNA-induced protein amyloidogenesis. Nucleic acids research *36*, 2249-2256.

Giraldo, R. (2007). Defined DNA sequences promote the assembly of a bacterial protein into distinct amyloid nanostructures. Proceedings of the National Academy of Sciences of the United States of America *104*, 17388-17393.

Giraldo, R., Andreu, J.M., and Diaz-Orejas, R. (1998). Protein domains and conformational changes in the activation of RepA, a DNA replication initiator. The EMBO journal *17*, 4511-4526.

Giraldo, R., Fernandez-Tornero, C., Evans, P.R., Diaz-Orejas, R., and Romero, A. (2003). A conformational switch between transcriptional repression and replication initiation in the RepA dimerization domain. Nature structural biology *10*, 565-571.

Giraldo, R., and Fernandez-Tresguerres, M.E. (2004). Twenty years of the pPS10 replicon: insights on the molecular mechanism for the activation of DNA replication in iteron-containing bacterial plasmids. Plasmid *52*, 69-83.

Giraldo, R., Moreno-Diaz de la Espina, S., Fernandez-Tresguerres, M.E., and Gasset-Rosa, F. (2011). RepA-WH1 prionoid: a synthetic amyloid proteinopathy in a minimalist host. Prion *5*, 60-64.

Heymann, J.B., and Belnap, D.M. (2007). Bsoft: image processing and molecular modeling for electron microscopy. Journal of structural biology *157*, 3-18.

Ivanova, M.I., Sievers, S.A., Sawaya, M.R., Wall, J.S., and Eisenberg, D. (2009). Molecular basis for insulin fibril assembly. Proceedings of the National Academy of Sciences of the United States of America *106*, 18990-18995.

Jimenez, J.L., Guijarro, J.I., Orlova, E., Zurdo, J., Dobson, C.M., Sunde, M., and Saibil, H.R. (1999). Cryo-electron microscopy structure of an SH3 amyloid fibril and model of the molecular packing. The EMBO journal *18*, 815-821.

Komori, H., Matsunaga, F., Higuchi, Y., Ishiai, M., Wada, C., and Miki, K. (1999). Crystal structure of a prokaryotic replication initiator protein bound to DNA at 2.6 A resolution. The EMBO journal *18*, 4597-4607.

Liu, C., Sawaya, M.R., and Eisenberg, D. (2011). beta(2)-microglobulin forms three-dimensional domain-swapped amyloid fibrils with disulfide linkages. Nature structural & molecular biology *18*, 49-55.

Lu, J.X., Qiang, W., Yau, W.M., Schwieters, C.D., Meredith, S.C., and Tycko, R. (2013). Molecular structure of beta-amyloid fibrils in Alzheimer's disease brain tissue. Cell *154*, 1257-1268.

Ludtke, S.J. (2010). 3-D structures of macromolecules using single-particle analysis in EMAN. Methods in molecular biology *673*, 157-173.

Mizuno, N., Baxa, U., and Steven, A.C. (2011). Structural dependence of HET-s amyloid fibril infectivity assessed by cryoelectron microscopy. Proceedings of the National Academy of Sciences of the United States of America *108*, 3252-3257.

Pettersen, E.F., Goddard, T.D., Huang, C.C., Couch, G.S., Greenblatt, D.M., Meng, E.C., and Ferrin, T.E. (2004). UCSF Chimera--a visualization system for exploratory research and analysis. Journal of computational chemistry *25*, 1605-1612.

Sachse, C., Grigorieff, N., and Fandrich, M. (2010). Nanoscale flexibility parameters of Alzheimer amyloid fibrils determined by electron cryo-microscopy. Angewandte Chemie *49*, 1321-1323.

Scheres, S.H., Nunez-Ramirez, R., Sorzano, C.O., Carazo, J.M., and Marabini, R. (2008). Image processing for electron microscopy single-particle analysis using XMIPP. Nature protocols *3*, 977-990.

Silva, J.L., Vieira, T.C.R.G., Gomes, M.P.B., Bom A.P.A., Lima, L.M.T.R., Freitas, M.S., Ishimaru, D., Cordeiro, Y., and Foguel, D. (2010). Ligand binding and hydration in protein misfolding: Insights form studies of prion protein and p53 tumor suppressor proteins. Acc Chem Res *43*, 271-279.

Sorzano, C.O., Marabini, R., Velazquez-Muriel, J., Bilbao-Castro, J.R., Scheres, S.H., Carazo, J.M., and Pascual-Montano, A. (2004). XMIPP: a new generation of an open-source image processing package for electron microscopy. Journal of structural biology *148*, 194-204.

Toyama, B.H., and Weissman, J.S. (2011). Amyloid structure: conformational diversity and consequences. Annual review of biochemistry *80*, 557-585.

Wang F., Wang, X., Yuan, C.G., and Ma J. (2010). Generating a prion with bacterially expressed recombinant prion protein. Science *327*, 1132-1135.

Wasmer, C., Lange, A., Van Melckebeke, H., Siemer, A.B., Riek, R., and Meier, B.H. (2008). Amyloid fibrils of the HET-s(218-289) prion form a beta solenoid with a triangular hydrophobic core. Science *319*, 1523-1526.

Wegrzyn, K., Fuentes-Perez, M.E., Bury, K., Rajewska, M., Moreno-Herrero, F., and Konieczny, I. (2014). Sequence-specific interactions of Rep proteins with ssDNA in the AT-rich region of the plasmid replication origin. Nucleic acids research *42*, 7807-7818.

Acknowledgements

This work was supported by grants of the Spanish Government SAF2011-22988 and the Autonomous Region of Madrid S2010/BMD-2316 to OL; BIO2012-30852 and

CSD2009-00088 to R.G.; BFU2011-25090 to J.M-B; and FIS2011-24638 and ERC StG ref 206117 to F. M-H.

ACCESSION NUMBERS

The EM maps have been deposited in the EM database with accession numbers: EMD-**** (for single filaments) and EMD-**** (for double filaments).

Figure legends

Figure 1. Structure of RepA-WH1 dimers and amyloid fibers

(A) Cartoon summarizing the functions of RepA in initiation of plasmid DNA replication and Rep-WH1 in the assembly of amyloid fibers.

(B) Structure of the RepA-WH1 dimer (PDB ID 1HKQ) (Giraldo et al., 2003). The sequence of RepA prone to acquire a β-structure is highlighted. Residue A31 is rendered space-filled.

(C) Negatively stained electron micrographs highlighting the hierarchical assembly of RepA-WH1. (i) Amyloid fibers growing from seeds made of purified globular RepA-WH1-mCherry aggregates generated in *E. coli* cytoplasm (Fernandez-Tresguerres et al., 2010). A black arrow indicates a fiber growing from a seed. (ii) RepA-WH1 fibers are polymorphic, both in terms of thickness and in their degree of twisting. (iii) Mechanical shearing in a buffer with reduced ionic strength results in fraying of fiber ends. Several filaments at the end of a fiber are highlighted within a box. (iv) Shearing ultimately

leads to dissociation of constituent filaments (one indicated, black arrow). Image enlarged respect to i-iii.

(D) CD spectra time-course of unseeded (i) and seeded (ii) RepA-WH1 aggregation. In ii, the inset shows the evolution of the ratio between the ellipticity values at 220 and 208 nm as an estimate of the preferential increase in β-sheet in the sample seeded with the intracellular, cytotoxic aggregates of the RepA-WH1 prionoid (continuous line) compared with the unseeded control sample (dashed line).

(see also **Figure S1**)

Figure 2. AFM analysis of RepA-WH1 fibers

(A) Typical AFM image of RepA-WH1 fibers. Two populations according to their heights were distinguished and their height profiles displayed on the right panel (taken in the direction of the arrow).

(B) AFM image of RepA-WH1 fibers disrupted by pipette shearing. Smaller filaments appear at the end of the fibers with mean heights of 3.9 ± 0.3 nm (see profile on the right panel). The color scale from dark to bright is 0 – 30 nm for all AFM images.

(See also **Figure S2** and **Table S1**)

Figure 3. 3D structure of RepA-WH1 filaments.

(A) Negative-staining electron microscopy of RepA-WH1 fibers and filaments. An electron microscopy field of fibers on incubation at day 15 shows a large frayed-fiber

(white arrow) and filaments of different length (black arrows). Scale-bar represents 100 nm.

(B) Top panel: gallery of images of RepA-WH1 filaments. Bottom panel: 2D-average images of RepA-WH1 filaments obtained after reference-free 2D classification and alignment. Scale bar = 50 Å.

(C, D) 3D structure of RepA-WH1 filaments. Left and right panels show the structures of single filaments (C, blue color) and double filaments (D, pink color) respectively. In each case, the structure is also shown as a transparent density where a model of monomeric RepA-WH1 (Giraldo and Fernandez-Tresguerres, 2004) has been fitted.

(E) Zoom image highlighting the density corresponding to a segment of the helix (left panel) in comparison to the density occupied by the atomic model of RepA-WH1 monomers (middle panel) or dimers (right panel) fitted into the EM map.

(See also **Figure S3**)

Figure 4. A schematic model for the hierarchical assembly of RepA-WH1 amyloids. Amyloidogenesis starts with the conformational change allosterically elicited by double-stranded DNA ligands on the stable soluble dimers (dWH1) to become metastable monomers (mWH1*) or, alternatively, with the conformational templating by pre-existing amyloid nuclei seeds. Monomers then assemble into single helical amyloid filaments, which are subsequently coiled as double helical filaments. Several of them associate side-by-side, and amyloid fibers are further twisted to variable degrees.

Figure1
Click here to download high resolution image

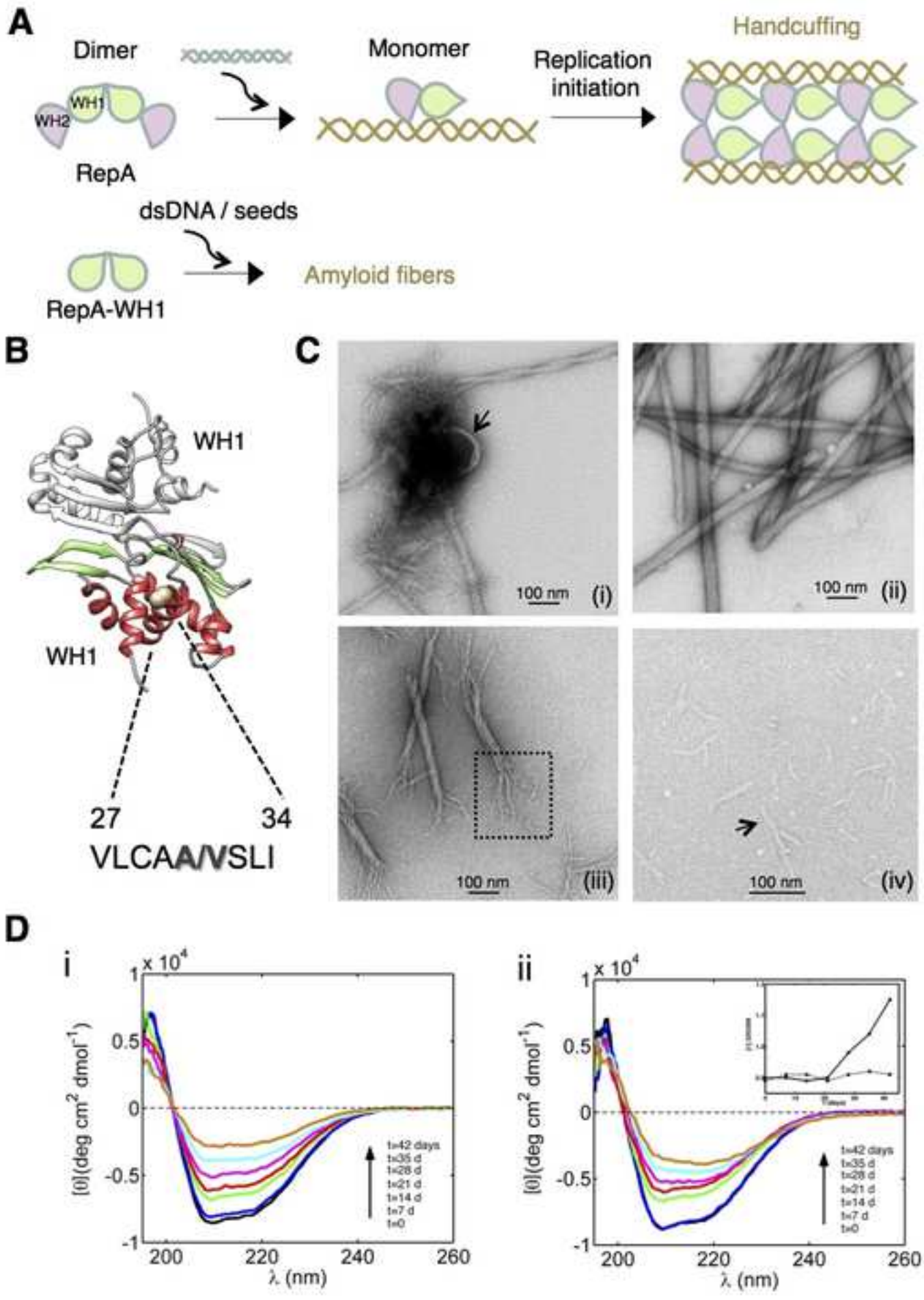

Figure2
Click here to download high resolution image

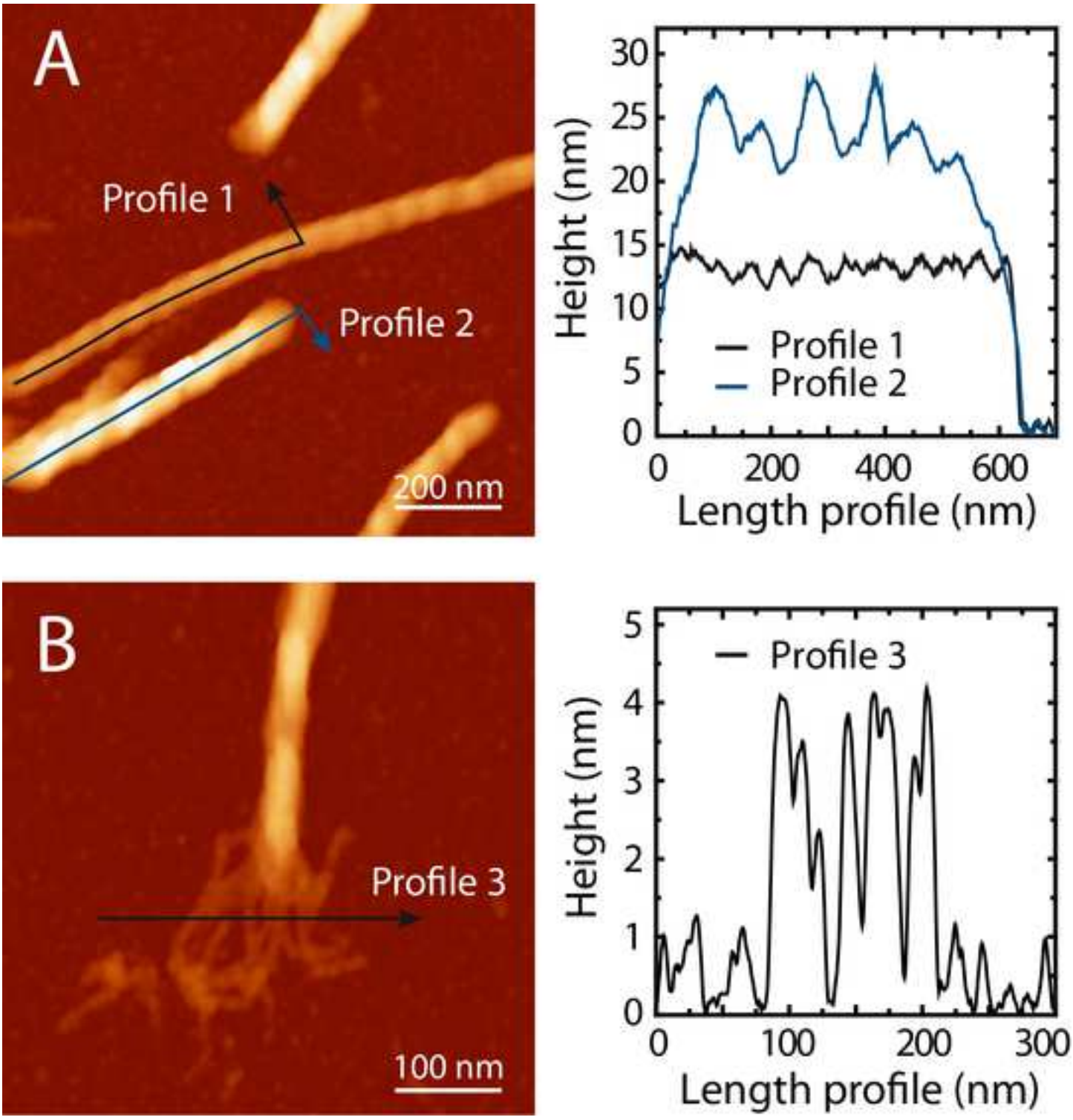

Figure3
Click here to download high resolution image

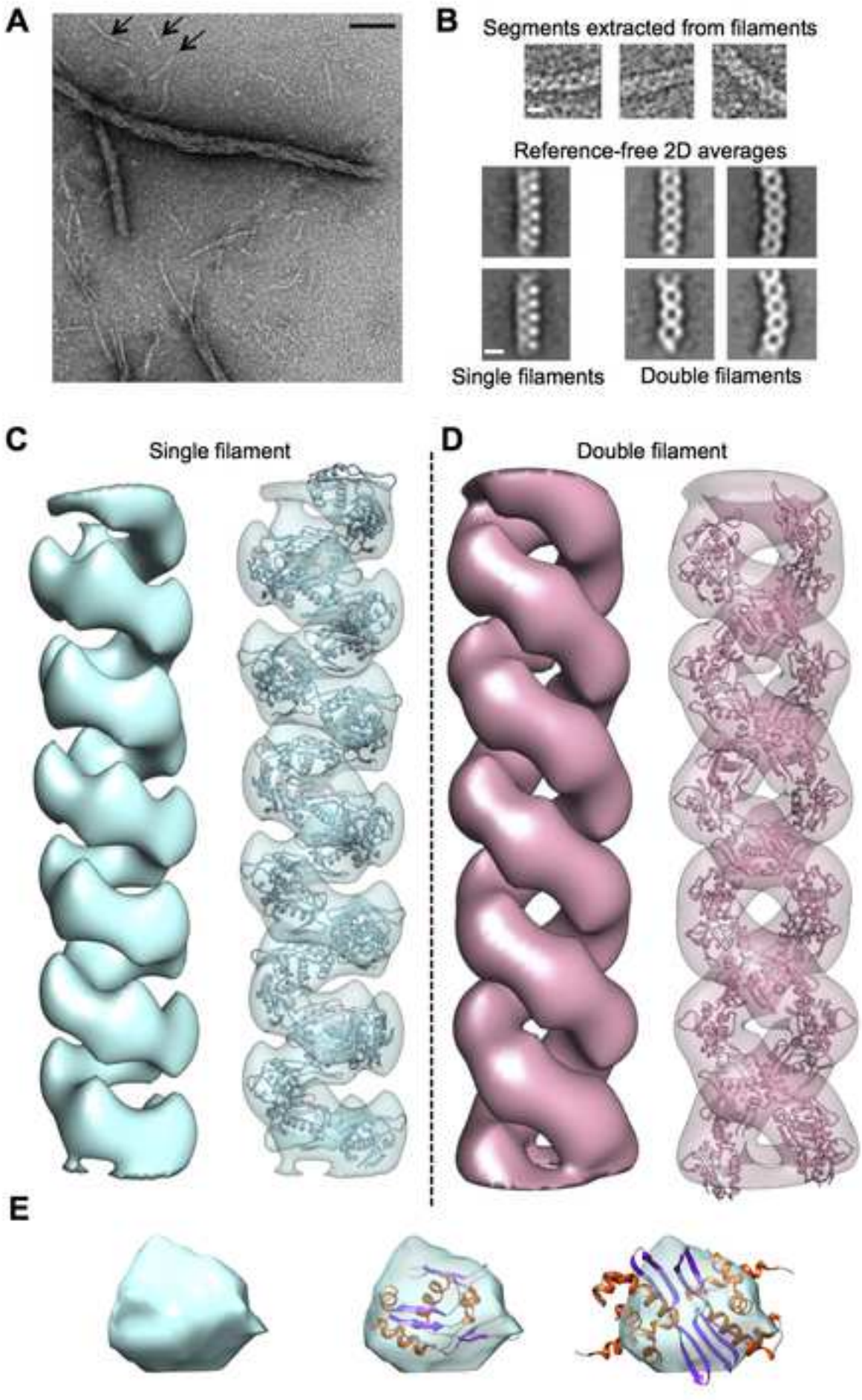

Figure4

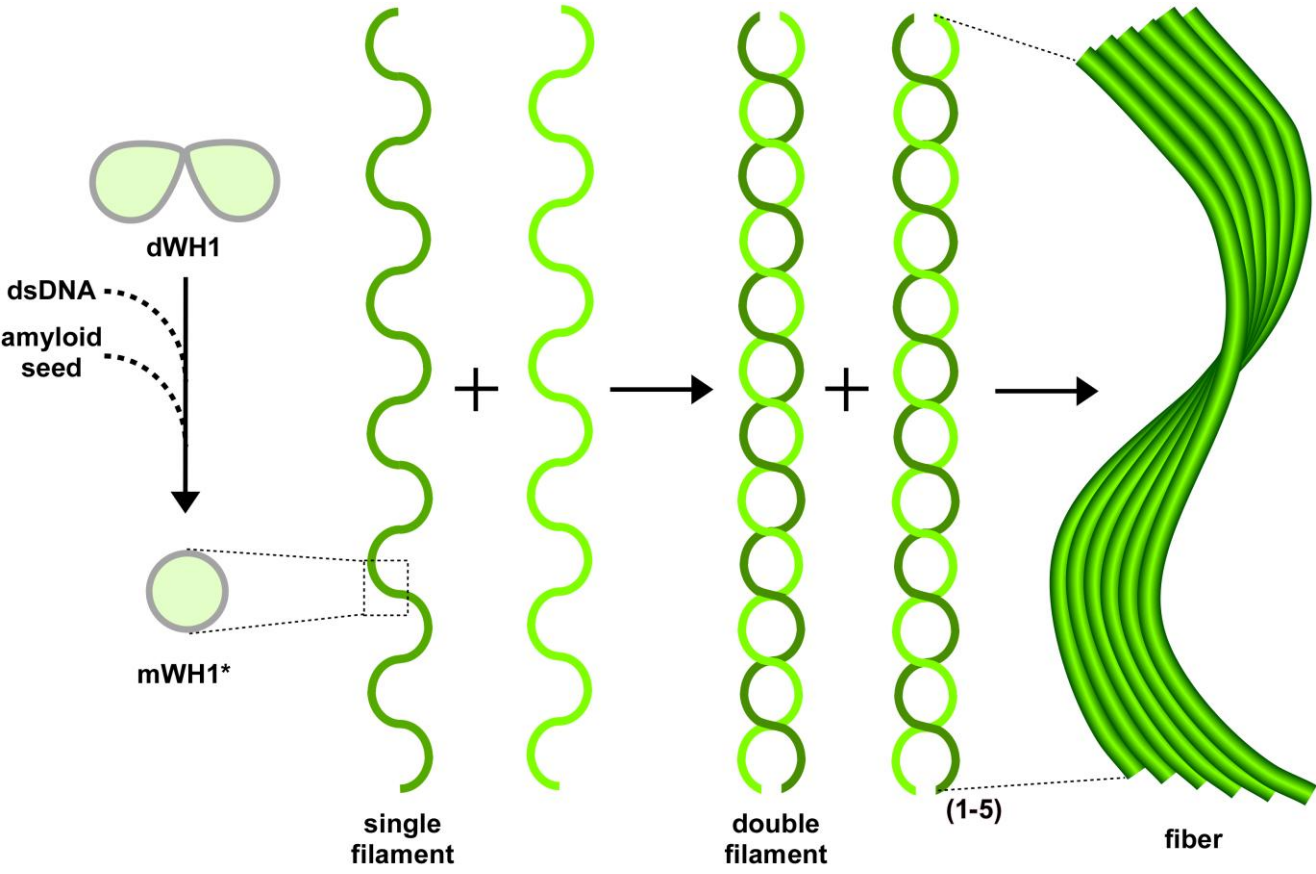
dWH1
dsDNA
amyloid
seed
mWH1*
single
filament
double
filament
(1-5)
fiber

SUPPLEMENTAL FIGURES AND LEGENDS

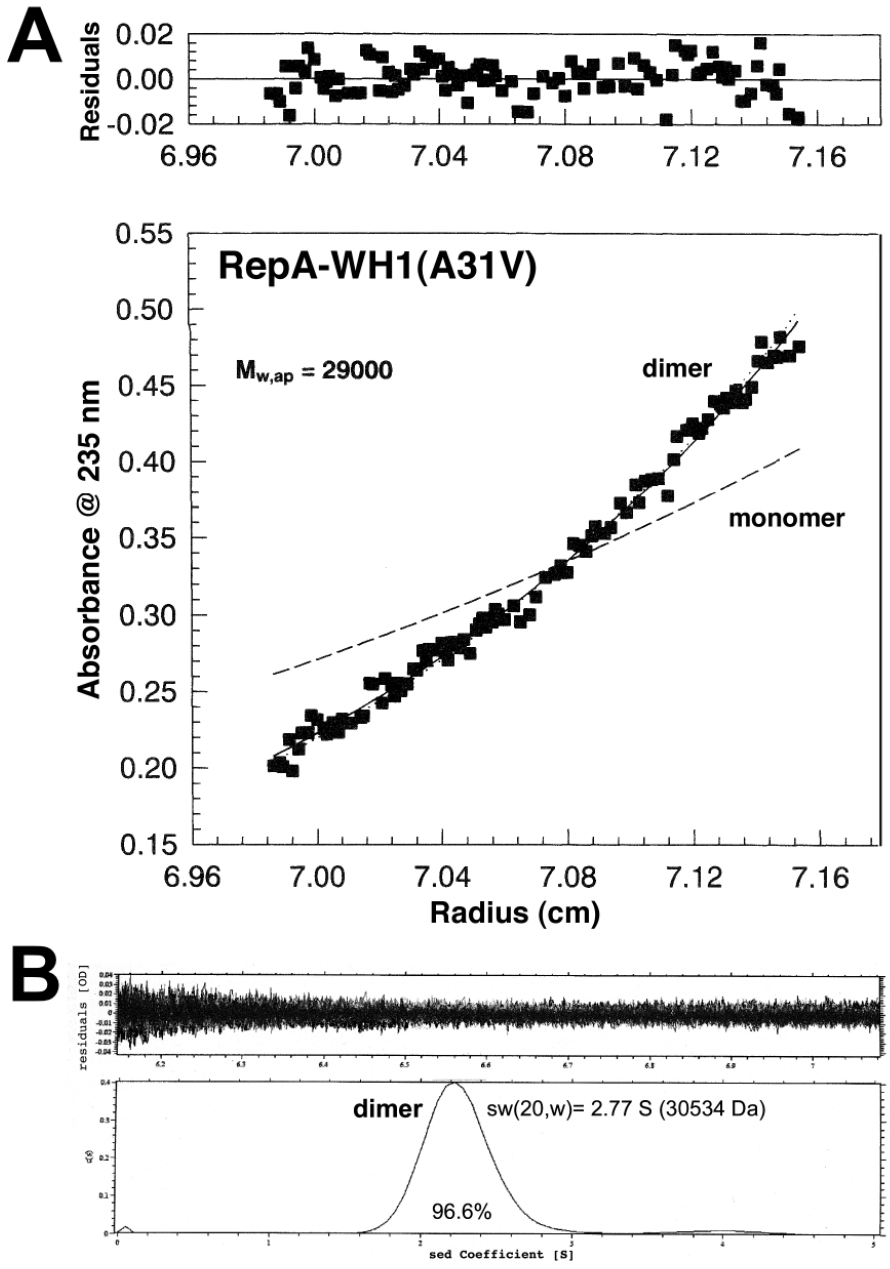

Supplemental Figure S1 (related to Figure 1). Purified RepA-WH1(A31V) is a dimer in solution, as revealed using analytical ultracentrifugation.

(A) Sedimentation equilibrium. Experiment was run at 14 μM protein concentration and at 12,000 rpm in a Beckman-Coulter XL-A analytical ultracentrifuge using the AN60Ti

rotor (12 mm optical length) at 20 ºC. Base line was acquired at 40,000 rpm. Continuous line represents the best fit of data to a dimer species at the sedimentation equilibrium, whereas dashed line represents the expected curve for a monomer.

(B) Sedimentation velocity. The experiment was performed on a protein sample at 5 μM. Run was carried out at 50,000 rpm in a Beckman-Coulter XL-I analytical ultracentrifuge in the same experimental conditions described in A. The distribution of sedimentation coefficients, as determined by the program SEDFIT (http://www.analyticalultracentrifugation.com/default.htm), fits to a nearly unique dimeric species (2. 77 S).

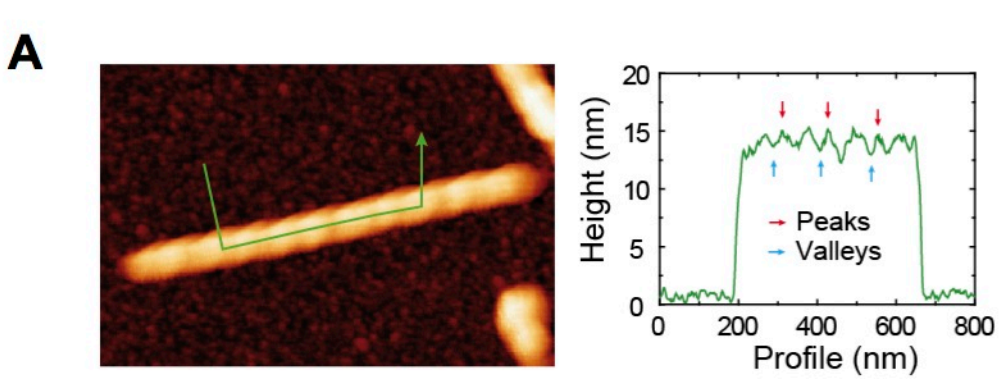
A
Height (nm)
Peaks
Valleys
Profile (nm)
B
For most abundant population:
For less abundant population:
filaments
Peaks
Valleys
fibers = 20
fibers = 5
Height (nm)
C
Profile 1
Profile 2
100 nm
1 nm
Profile 1 (nm)
Profile 2 (nm)

Supplemental Figure S2. AFM measurements of the fibers (related to Figure 2).

(A) From each fiber, three characteristic measurements were taken from the height profile for the peaks and valleys, respectively. The fibers selected were those in which the helicity was visible as shown in the Figure 2A or in this following example (colour scale of the image from dark to white is 0-20 nm). Broken fibers without a clear helicity pattern were discarded (aprox. 30%).

(B) All the data was represented in a height histogram and the mean value and the standard deviation obtained for each population calculated.

(C) Height and lateral calibrations of the AFM measurements were performed with commercial grids as described in the Experimental Procedures section. In addition, we used DNA molecules as standard particles for calibration of the height and X and Y directions. As an example, the figure shows height profiles across a DNA molecule (colour scale in the Figure from dark to white is 0-2 nm).

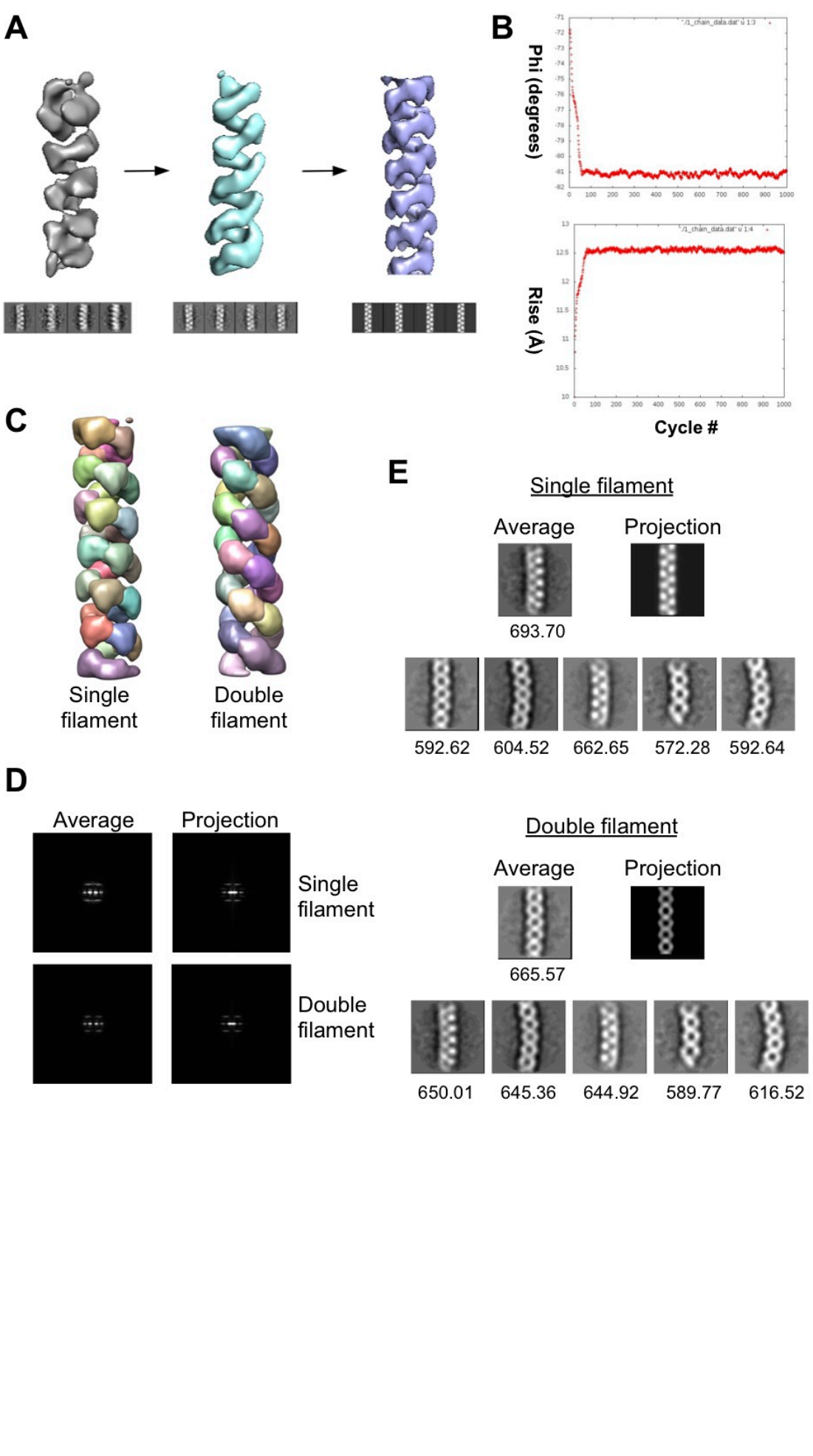
A
B
Phi (degrees)
Rise (Å)
Cycle #
C
Single filament
Double filament
D
Average
Projection
Single filament
Double filament
E
Single filament
Average
Projection
693.70
592.62
604.52
662.65
572.28
592.64
Double filament
Average
Projection
665.57
650.01
645.36
644.92
589.77
616.52

Supplemental Figure S3. Structural analysis of single and double filaments by EM (related to Figure 3).

(A) Helical processing flowchart. Top panel: 3D reconstructions obtained with EMAN (left and middle volume) for the preliminary determination of helical parameters. The volume to the right corresponds to the single filament structure shown in Figure 3 at a lower threshold. Bottom panel: 2D projections for each 3D structure.

(B) Example of convergence curves of angles (top panel) and helical rise (lower panel) obtained in the refinement during the Iterative Helical Real Space Reconstruction protocol.

(C) Output of the segmentation of single and double filaments using UCSF Chimera (Pettersen et al., 2004). Each segment is represented with a different color.

(D) Comparison between the power spectrum of average images and projections from the 3D structures of single and double filaments.

(E) Projections of a single and double filament were compared with a collection of average images of both types of filaments that were never used for refinement (refinement used only filament images and not their averages). This comparison was performed using the *refine* command in EMAN and a quality factor defined by EMAN scored the quality of the match, with higher values indicating a better match (Ludtke, 2010). We observed that projections of the final 3D structures matched better with reference-free averages obtained from those images corresponding to the sub-class used in the reconstruction (top row in the panel for single and double filaments), compared to

the scores obtained with other similar averages but corresponding to slightly different conformations.

SUPPLEMENTAL TABLE

Table S1. Height variability observed in both populations of fibers. We analysed 20 and 5 fibers for the most and less abundant population of fibers, respectively.

# Fiber	Peak 1	Peak 2	Peak 3	Valley 1	Valley 2	Valley 3
1	15.1	15.6	15.4	12.8	13.8	13.3
2	14.5	14.6	14.9	12.8	13.3	13.4
3	14.7	18.6	16.7	12.6	13.9	12.9
4	16.8	18	17.5	15.2	15.2	15.1
5	15.4	15	13.8	13.5	13.1	12.3
6	15	16.3	17.1	13.2	12.4	13.7
7	14.6	14.6	13.8	13.1	13.2	12.6
8	18.5	17.9	16.6	15.3	13.4	12
9	18.4	17.8	15.8	12.8	12.2	12.7
10	14.1	14.3	14.7	11.8	12.3	12.3
11	15.8	15.9	15.6	14.1	13.6	14
12	13.7	14.6	14.2	12.4	12.8	12.3
13	13.3	13.8	13.6	11.2	12	12.1
14	14.9	16.2	16.4	13.3	14.2	13.2
15	14.7	15.3	15.7	13.8	12.7	12.6

16	13.7	13.2	14	12.2	11.9	10.6
17	16.5	18.5	19	15.7	16.6	15.3
18	15.3	15.9	15.5	12.2	13.3	13.5
19	14.3	14.8	14.7	12.2	12.7	11.7
20	16.9	15.8	17.3	13.8	14.1	13.9

For the less abundant population of fibers

# Fiber	Peak 1	Peak 2	Peak 3	Valley 1	Valley 2	Valley 3
1	23.6	24.7	23.6	21.4	19.9	21.6
2	25.7	26.5	23.5	20.8	21.1	20.2
3	25.9	25.9	27	20.4	22.9	20.7
4	23.2	24.6	23.5	22.6	21.2	20.8
5	24.9	25.1	25.5	20.5	20.3	19.9

Height variability observed in both populations of fibers. We analysed 20 and 5 fibers for the most and less abundant population of fibers, respectively.

Supplemental Figure S1. We used analytical ultracentrifugation to demonstrate that purified RepA-WH1(A31V) is a dimer in solution (This is related to Figure 1).

Supplemental Figure S2. The figure shows all AFM measurements of fibers (This is related to Figure 2).

Supplemental Figure S3. Supporting information about the structural analysis of single and double filaments by EM (This is related to Figure 3).

Supplemental Table S1. This table shows values of height variability observed in both populations of fibers, as measured by AFM (This is related to Figure 2).